



USB-powered technology platform for laser ablative thrust generation

TONI BAUER, SEBASTIAN WEIXLER, RAOUL-AMADEUS LORBEER,*  AND HANS-ALBERT ECKEL

Institute of Technical Physics, German Aerospace Center (DLR), Pfaffenwaldring 38-40, 70569 Stuttgart, Germany

*raoul.lorbeer@dlr.de

Abstract: Small satellites gave the opportunity to universities all over the world, allowing their students to participate in a complete satellite mission. After some years, the graduating students and the developing technologies for satellites as small as a 1 liter cube, have reached a point where a new type of space industry is developing and gaining importance. Despite all possibilities and components available for such systems, it is still a very difficult task to maneuver these satellites due to the lack of compact and efficient thruster systems. Here we demonstrate the compactification of a laser ablative thruster concept called MICROLAS. We verify the functionality of all sub components and demonstrate ablation under vacuum conditions.

Published by The Optical Society under the terms of the [Creative Commons Attribution 4.0 License](https://creativecommons.org/licenses/by/4.0/). Further distribution of this work must maintain attribution to the author(s) and the published article's title, journal citation, and DOI.

1. Introduction

Laser systems with high beam quality and beam steering capabilities are relevant to a large number of applications such as laser micromachining [1–4], laser ranging [5,6], imaging [7,8] and communication [9,10]. Our research is focused on the use of the ablation of material as a source of thrust [4,11–14]. In this paper we will elucidate laser ablative propulsion in the context of small satellite navigation.

With the small satellite market gaining momentum, the research for small electric thrusters became more and more prominent, too [15]. For our MICROLAS concept on the other hand [13,14], we were planning to create a technology demonstration platform, suitable to answer the question of the implementability of laser ablative thrusters. In the early development phase of this process we realized that this demonstration platform could just as well be referred to as an electrical micro-propulsion system, with dimensions fitting inside a cube-sat.

With these nano-satellite constraints we were able to integrate a system with a volume of less than $10 \times 10 \times 5 \text{ cm}^3$ which is able to perform three-dimensional scanning laser ablation of different materials controlled and powered via a regular USB-Port.

The constraints dictated by a 1U cube-sat system and a laser ablative thruster can be summarized by an electrical power consumption below 2 W, a volume not surpassing the outer dimensions of a 1U-sat while leaving at least half of the volume to other essential hardware, no moving parts, less than 300 g of mass in total, more than 1 cm^3 of addressable propellant and laser fluences above 10 J/cm^2 . The generation of torque was neglected since modern cube-sat systems are able to utilize e.g. magnetic torquers [16] to compensate for residual torque prior, during and after the manoeuvre.

These parameters lead to the selection of several core technologies which needed to be combined. First of all, tapered laser diodes which offer a high efficiency of up to 60 % combined with a high beam quality. These, therefore, allow to reach fluences suitable for laser ablation [17–19]. Furthermore, liquid lenses are capable of shifting the focal length for scanning in longitudinal direction, with little moving mass, a small form factor and low power consumption

while preserving the beam quality [20,21]. Moreover, 2D MEMS scanning mirrors providing a very small and energy saving method of lateral beam scanning by moving a small mirror mass. Additionally, they are already used for building integrated optical devices in automotive and medical laser scanning applications [22,23].

To combine all electrical components, it was necessary to introduce custom printed circuit boards (PCB), DC/DC power converters and a micro-controller. Mechanical components were created using additive manufacturing. 3D-printing allowed to create a compact optical and electrical assembly while keeping all tolerances small enough to create a functioning optical device.

2. Materials and methods

2.1. Optical components and design

Figure 1 shows the optical design of the system simulated with Zemax OpticStudio 16.2. In order to achieve the highest possible laser fluence for ablation on the target surface (11) for an average electrical power consumption of less than 2 W the spot size has to be minimized. Therefore, a laser source with a high beam quality as well as high efficiency is needed. We decided to use a tapered laser diode (1) (Dilas TL-0976-5000), which has a specified efficiency of up to $\eta \approx 60\%$ and a high beam quality of typically $M^2 = 1.7$ and below $M^2 = 2.6$ at maximum power as well as a wavelength of $\lambda \approx 980$ nm. The beam is collimated by an aspheric lens (2). Astigmatism correction is realized using a cylindrical lens (3), while an anamorphic prism pair (4) is used to turn the elliptical beam profile into a circular beam profile. A custom made aspheric lens (6) with 25 mm focal length corrects static aberrations of the system. The focal length is adjusted using a liquid lens (5) (Varioptic (Parrot) Arctic 39N). The beam can be deflected up to $\pm 4^\circ$ on both lateral axes with a 3.6 mm diameter MEMS mirror (7) (Mirrorcle A7B2.1-3600AU). To prevent contamination and damage to the optical components by ablated material the image of the MEMS mirror (i) is laterally shifted by several millimeters using a toroidal mirror (8). The use of a toroidal mirror results in a tilted scanning plane (11) relative to the laser beam. Additionally, the system is protected by a glass cover slip (10). A second mirror (9) folds the beam path of the optical system to keep its footprint smaller than 10×10 cm².

2.2. Optomechanics

The opto-mechanical assembly is depicted in Fig. 2. The monolithic optic mount (blue) was manufactured using an Ultimaker 3 extended 3D printer with Ultimaker PLA material. All mounting positions are adapted to their corresponding components and define its position and orientation. The laser diode is mounted independently on a copper sub mount which is soldered onto the underlying PCB and serves as heat sink and anode contact. The opto-mechanical assembly and the laser-diode relative to each other as well as the orientation of the cylindrical lens are adjustable. This is achieved with threaded bushings and fine hex screws.

2.3. Electronics

The electronics of the device were developed in three modules. The Laser-board contains the main circuit board with micro controller and laser diode driver electronics, the lens-board supports the liquid lens driver electronics and the scanner-board supports (resonant) MEMS-scanner driver electronics.

2.3.1. Laser-Board

Contains an Atmel SAMD21G18A micro controller (μ C). This chip is compatible to the Arduino IDE and the board can be powered and controlled via Micro USB or Serial Wire Debug (SWD). The liquid lens and the MEMS scanner are controlled by the μ C via an I²C-bus and pulse width

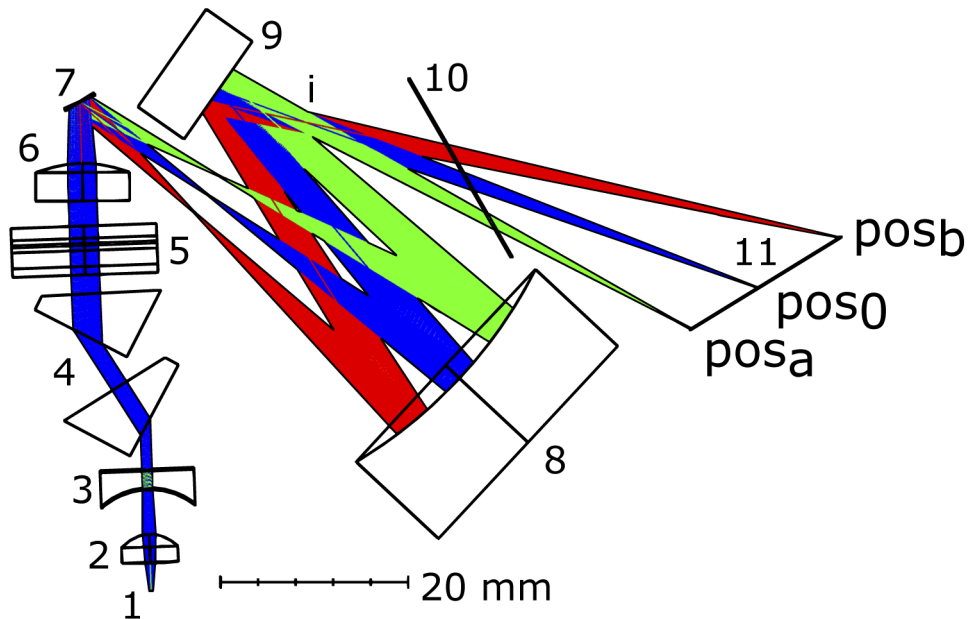


Fig. 1. Zemax-model of the optical setup with optical components (black) and beam path for 0° (blue) and $\pm 4^\circ$ (green and red) MEMS mirror deflection angle. Optical components: (1) laser diode, (2) collimation asphere, (3) cylindric lens, (4) anamorphous prism pair, (5) liquid lens, (6) correction asphere, (7) MEMS-scanner, (8) toroidal mirror, (9) plain mirror, (10) safety glass and (11) propellant plane. The real image of the MEMS-scanner is situated at (i). Three positions ($pos_{0,a,b}$) for different scanner tilt angles are indicated.

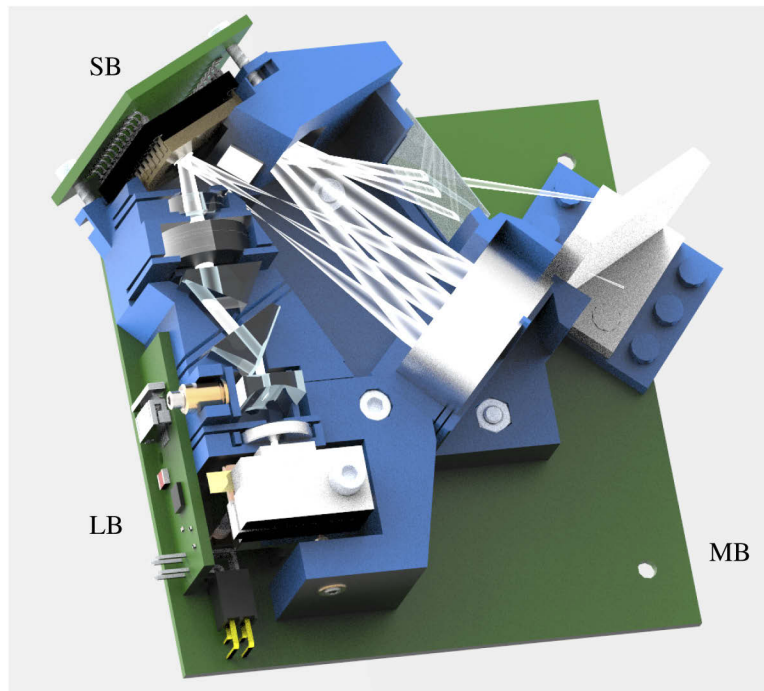


Fig. 2. Full assembly of the module: Laser-board (motherboard) (MB), optic mount with positioning arm (blue), lens-board (LB) and scanner-board (SB).

modulation (PWM) respectively. The laser driver is designed to allow pulsed operation of the laser diode at repetition rates of 100 Hz to 10 kHz with pulse lengths of $1 \mu\text{s}$ to $100 \mu\text{s}$ and a voltage of 900 mV to 2000 mV. The electrical energy for the laser pulses with an optical peak power of up to 4 W is stored in a capacitor stack which is loaded with a voltage regulated buck converter. Square current pulses are realized using a half bridge driving two high power mosfets.

2.3.2. Lens-Board

Converts the 3.3 V power supply to pulses of up to 62 V to drive the liquid lens.

2.3.3. Scanner-Board

Drives the MEMS scanner with resonant PWM signals. There are two independent signals for each axis that are electrically converted up to 24 V.

Further technical details and documentation on electronics, optics and mechanics may be requested from the corresponding author.

2.4. Characterization

The electro-optical components were characterized in order to ensure that they meet the system requirements.

The image quality and possible focal lengths of the liquid lens were determined by measuring its Modulation Transfer Function (MTF). Therefore, a sector star test target (Thorlabs R1L1S3P) illuminated by an LED-Cluster (Kingbright BL0106-15-28) through a diffuser (Thorlabs DG10-220-B) and an Edmund Optics $975 \text{ nm} \times 50 \text{ nm}$ OD4 band pass filter was imaged through the liquid lens and an asphere (Thorlabs AL1815-B) into a camera (Basler ace 2000) with a 75 mm camera lens (Fig. 3 a)). Different lens voltages and the camera trigger were controlled with an Arduino M0 Pro Board to take pictures for lens voltages of 20 V to 62 V in steps of 0.5 V. Using the free software ImageJ, the pictures were transformed into polar coordinates and then (Fourier) band pass filtered at the sector star's angular grid frequency. Finally, the standard deviation of the grey values depending on the radius, which defines the grid frequency, can be determined and normalized to find the MTF for every lens voltage. The distance d between the sector star and the asphere was variable in order to examine the focal length and image quality of the liquid lens depending on the voltage.

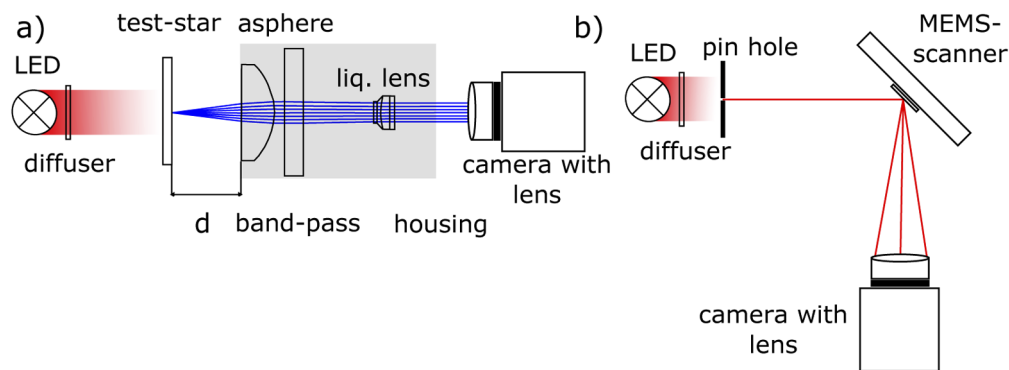


Fig. 3. Schematic testbeds for a) liquid lens characterization and b) MEMS-scanner characterization.

The MEMS scanner's deflection angle and possible scan patterns with two axes resonant operation were studied by imaging a $50 \mu\text{m}$ pin hole illuminated by a LED-Cluster (Kingbright

BL0106-15-28) through a diffuser (Thorlabs DG10-220-B) over the scanner mirror into the Basler ace 2000 camera with a 12.5 mm/F1.4 (Navitar) camera lens (Fig. 3 b)).

The optical output power of the system was measured directly after the collimation and beam forming optics (Fig. 1 (1) through (4), without liquid lens, correction asphere and MEMS scanner) and at the possible target surface of the fully assembled system using an Ophir 3A power meter with the Pulsar interface and the included software. The average optical power was measured and averaged over 30 s for repetition rates of 100 Hz, 1 kHz and 5 kHz, voltages up to 1550 mV. Furthermore, the pulse length was set to 1 μ s, 10 μ s and if possible 50 μ s as well as 90 μ s.

In order to prove and quantify laser ablation at the target the system was mounted in a vacuum chamber with a Rode NT1 microphone mounted at a distance of ca. 2 cm from the target surface to detect ablated material. The power supply was realized using a power bank (PNY P-B5200-2CURK-RB) with time controlled operation of the system as shown in Table 1 at atmospheric pressure and at fine vacuum down to 1.5×10^{-3} mbar. For the ablation experiments we used charcoal. Bike tire rubber and a mixture of caramel color and printing ink dried for several days were tested as well and showed ablation, which makes them propellant candidates in future investigations. All these materials have a high absorption at the laser wavelength and a low thermal conductivity to keep the energy density in the focus as high as possible over the pulse duration. A blind test was performed with defocused laser light directly before the actual ablation tests. Laser parameters for vacuum test were fixed to 826 pulses per second, 40 μ s pulse duration and a driving voltage of 1.54 V corresponding to an optical peak power of 3.4 W (compare results section). This leads to 136 μ J of pulse energy after the prism pair. An additional 22% to 25% of additional losses from the remaining components (5-10) before reaching the target (11) (compare Fig. 1) were determined experimentally.

Table 1. Automatic operation command list for vacuum ablation measurement.

time from startup [s]	command	function
113	field 3 0.5 0.5	starting laser synchronous scan
116	pulse 826 40 1540	starting laser with $f = 826$ Hz, $\tau = 40$ μ s and $U = 1540$ mV
120	lval U	focusing on target plane with liquid lens ($U = 41$ V to 42.5 V)
130	shutdown	shutdown
wait 13 s (23 s every 3rd and 33 s every 5th round), restart from t = 113 s		

3. Results

3.1. Optical System Simulations

Even though the laser source itself does not yield a perfect M^2 beam quality, the optical system was designed to create the best focal spot quality possible with the given size constraints. Figure 4 shows spot diagrams generated with Zemax Optic Studio, on the tilted and curved surface of the focal scanning plane addressable with the MEMS-mirror. Single dots indicate the position at which a ray-traced beam crosses this surface. The black circles indicate the diameter of the airy disc expected by the simulation tool. The tilted geometry of the focal scanning plane, results in the asymmetric expansion of several rays beyond the airy diameter. Further parameters deduced from the simulations are summarized in Table 2.

These simulation results have to be put into the context of the abilities of the simulation. Image position is given relative to the plane of the tilted surface. The airy radius is an estimation generated from the ray tracing algorithm. It does not appear to account for the angle of incidence (AOI) of the beam, which would lead to an elliptical shape. The RMS radius of the spot diagrams does not account for asymmetries neither. Nevertheless, as an indicator the RMS radii are consequently smaller than the expected airy radii. Therefore, an optical quality very close to

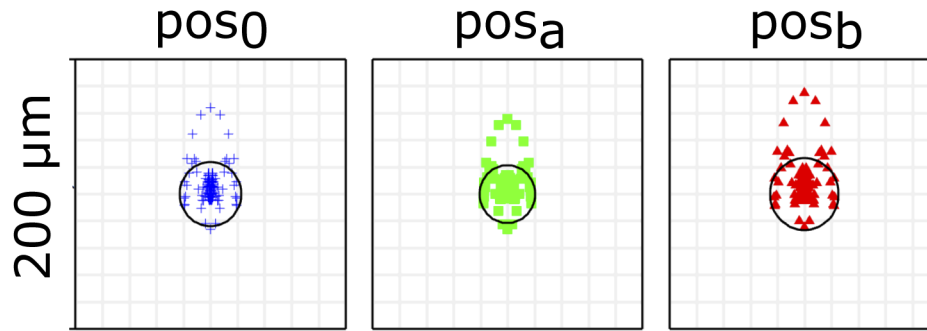


Fig. 4. spot diagram from simulations with Zemax Optic Studio for positions $pos_{0,a,b}$ as indicated in Fig. 1. Shown are the intersections of the ray-tracing rays with the focal scanning plane roughly coinciding with the propellant plane (11) in Fig. 1. Circles indicate the expected airy diameter

Table 2. Simulated optical beam properties for positions $pos_{0,a,b}$ as indicated in Fig. 1. A top head beam was assumed.

property	pos_0	pos_a	pos_b
image pos_y [mm]	0.143	-9.259	10.998
airy radius [μ m] from spot diagram	23.22	20.96	25.92
RMS radius [μ m] from spot diagram	14.6	12.64	17.33
Strehl ratio from Huygens PSF	0.98	0.98	0.97
AOI [$^\circ$] curved surface	45.11	42.35	46.75
AOI [$^\circ$] flat surface	45.19	37.03	53.07
focal NA	0.026	0.028	0.023
80 % encircled energy radius [μ m]	18.70	16.89	21.09
fluence per pulse energy [J/cm ² per 1 μ J]	0.073	0.089	0.057
power density per laser peak power [kW/cm ² per W]	73	89	57

aberration free results may be expected. This is supported by the results from the "Huygens PSF" method which allows to deduce the "Strehl ratio" (SR) of the beam. A SR of 1.0 represents a perfect optical system. Here again the simulation results suggest that the simulation does not account for a tilted AOI. Nevertheless, we believe these results to be true for a hypothetical vertical (0°) AOI. Due to the small numerical aperture (NA) of the beam, the Rayleigh length is significantly larger, than the spot diameter. Therefore, we will assume a purely geometrical distortion of the focal spot due to differing AOI in our succeeding considerations. Even though we utilized a flat target surface in our experiments, a curved surface appears to be beneficial due to two effects. First, the system has the smallest possible spot diameter in all positions and second the AOI on the curved surface does differ by less than 5° for changing positions (compare Table 2).

To deduce expectations for the achievable fluence the radii encircling 80% of the deposited energy were calculated. The corresponding average fluence per emitted μ J is displayed as "fluence per pulse energy" in Table 2. Correspondingly, the power density per laser peak power is displayed as well.

3.2. Liquid lens characterization

Figure 5 shows the MTF of the liquid lens test system with a distance of $d = 10.95$ mm between target and aspheric lens from measurements and Zemax simulation. The x-axis shows the

lens voltage and the y-axis shows the lattice frequency while the MTF is coded in color. The whole setup was simulated with Zemax using data provided by the manufacturer, neglecting the objective lens in front of the camera. At the lens voltage with the highest MTF values the target is in focus for the particular distance d . Within the measurable range from 20 to 100 lines/mm the measurement reproduced the simulation with an MTF offset of approximately -0.07.

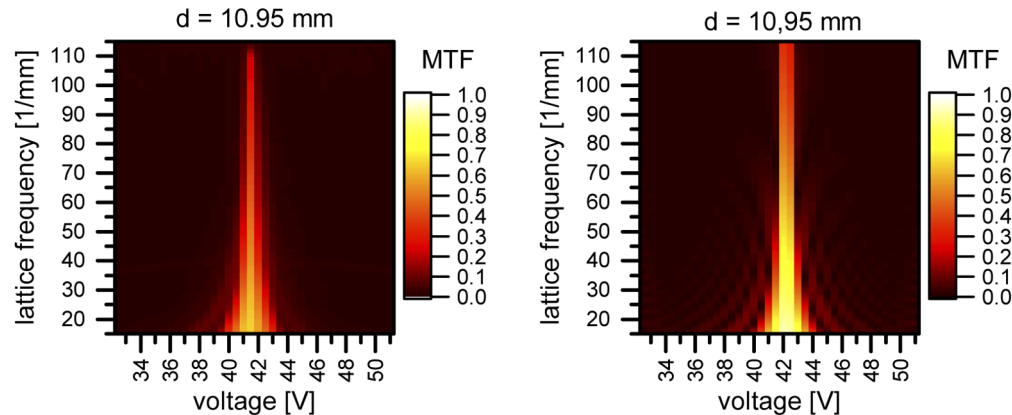


Fig. 5. Modulation transfer function of the liquid lens test setup for different lens voltages. left: Measurement, right: Simulation

By repeating the measurement for different distances, the focus shift possible with this liquid lens was found to be 6.5 mm compared to 5.5 mm in the simulation (parameter d in Fig. 3 a)). This also allowed to address the "protective glass cover slip" (Fig. 1 (10)) to ablate and clean the window from residual propellant deposited by the ablation process. The power consumption of the lens board increases linearly with lens voltage from approx. 20 mW at 9.8 V to approx. 69 mW at 62 V.

3.3. MEMS scanner operation

For the resonant MEMS scanner operation the scanner's natural oscillation parameters - resonance frequency f_0 and damping time $t_0(1/e)$ - had to be determined. Figure 6(a) shows the decay curve of the MEMS scanner's x-axis oscillation after switching off a 413 Hz rectangular excitation with 12 V amplitude. Fitting a damped harmonic oscillator to the curve results in a resonance frequency of $f_0 = 413.3$ Hz and a damping time of $t_0(1/e) = 27.4$ ms. This equals a quality factor of 5.6. Figure 6(b) shows the maximum amplitude of the MEMS scanner deflection angle depending on the PWM duty cycle for 24 V excitation and a frequency of 413 Hz on both axes. The fitted curves consist of the sum of the first and third harmonic sine waves. Deflection angles of $\pm 4.13^\circ$ (x-axis) and $\pm 3.57^\circ$ (y-axis) have been reached.

Controlling duration and phase of the PWM signals allows to scan all possible elliptical Lissajous figures. The original idea was to scan circles or spirals on the target surface to uniformly remove the material. At the maximum deflection angle the circumference of the scanned circle is approximately 5 cm. Scanning at the resonance frequency of 413 Hz results in an effective scan velocity of $20.65 \mu\text{m}/\mu\text{s}$. In the Zemax simulation the spot size was $40 \mu\text{m}$ (compare Table 2) which means that over a $10 \mu\text{s}$ pulse the spot is scanned over the area of 5 spots, making the fluence on the target decrease by a factor of 5. To avoid this loss we implemented a laser synchronous scan. In this mode both axes oscillate in phase to scan a line. The laser is operated at a repetition rate of 826 Hz to emit one pulse at each turning point of the sinusoidal scanner oscillation when the velocity is minimal. By controlling the amplitude with the PWM duty

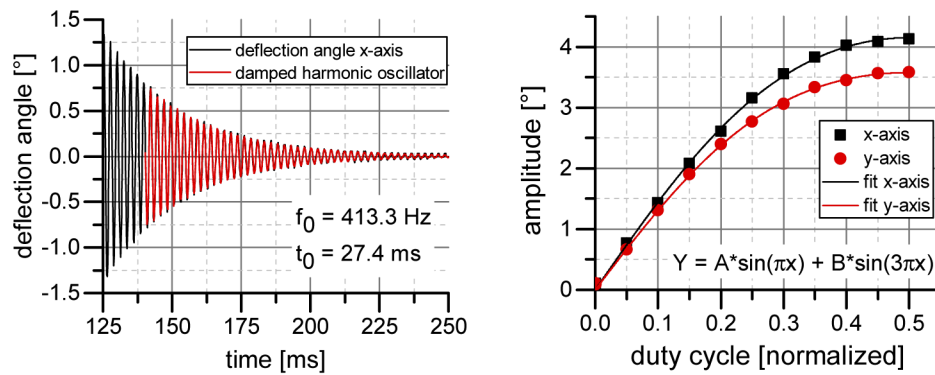


Fig. 6. Resonant MEMS scanner characterization. The standard deviation of the measured deflection angles is smaller than 0.04° (1 px on the camera sensor) and therefore not visible in the graphs. left: Decay curve of resonant MEMS-scanner oscillation after 12 V excitation. right: Maximum MEMS-scanner amplitude in resonant mode depending on PWM duty cycle. With $A_x = 4.29$, $B_x = 0.14$, $A_y = 3.76$, $B_y = 0.18$.

cycle the turning points can be scanned over the target plane. The power consumption of the scanner-board is limited to 240 mW by design.

3.4. Laser diode

The average and peak optical power of the system measured behind the collimation and beam forming optics are depicted in Fig. 7. The error bars correspond to 3% measurement error of the power meter as specified by the manufacturer. At the target plane, a maximum peak power of 2.82 ± 0.09 W was measured at 1530 mV, a repetition rate of 1000 Hz and $10 \mu\text{s}$ pulse length. The highest average optical power measured was close to 180 mW at $50 \mu\text{s}$ pulse duration and 1.53 V driving voltage. Consulting the specifications of the laser diode this corresponds to 5 A peak laser diode current and therefore a power draw close to 400 mW. Additionally, the laser-board had a basic power consumption of 140 mW.

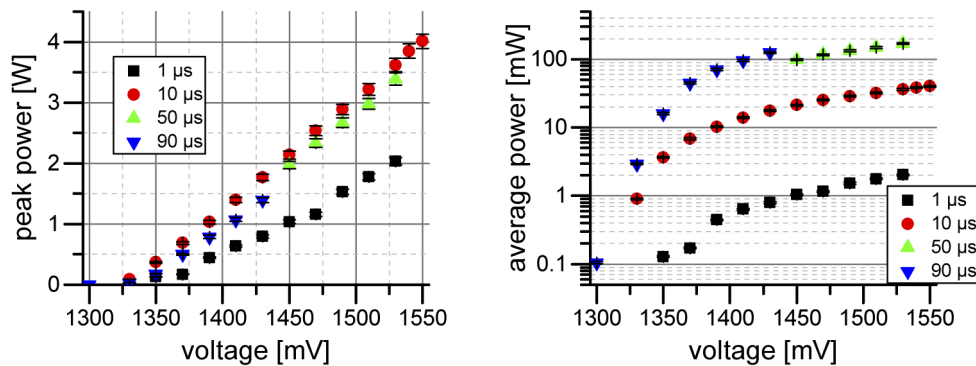


Fig. 7. Laser power after the prism pair depending on voltage and pulse length at a repetition rate of 1 kHz. left: peak power right: average power

3.5. Ablation detection

In ablation experiments with the system at atmospheric pressure, ablation with emission of visible (red and white) light as well as acoustic signals during the process and the removal of target

material could be observed for the three target materials (compare [Visualization 1](#) [24]). In order to prove that there is a laser ablation process and not only a combustion of target material with atmospheric oxygen, the experiments had to be performed under vacuum conditions. Charcoal was investigated further due to the high vaporization temperature of graphite and therefore the expected specific impulse of at least 100 s.

Figure 8 shows the spectrogram of the microphone channel at a pressure of 2 to 3×10^{-3} mbar. As shown in [Table 1](#) the laser was operated for periods of 10 s with breaks of different lengths in between to correlate the signals from the microphone with the laser operation. After every peak, which is not a multiple of 3 or 5 (82, 83, 86, 88, 89) there is a break of 20 s in laser operation. After peaks 81, 84 and 87 as multiples of 3 there are breaks of 30 s and after peak 80 and 85 as a multiple of 5 there is a break of 40 s shown by a corresponding pause in the measured signals.

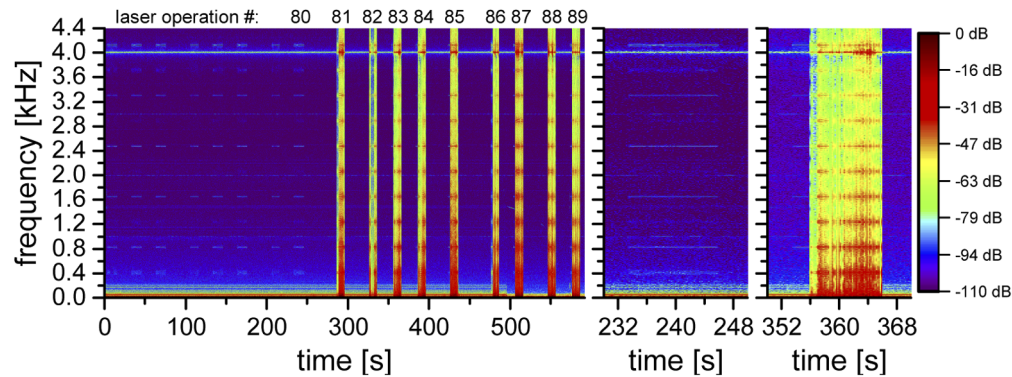


Fig. 8. Spectrogram of audio stream generated during vacuum ablation test at a pressure between 2 to 3×10^{-3} mbar. Left: Overview of the 600 s measurement. Middle: Enlarged blind test with liquid lens tuned away from the propellant plane. Right: Enlarged ablation test. At second 356 the liquid lens adjusts to the focal plane.

While recording the depicted data the pressure in the vacuum chamber was between 2 and 3×10^{-3} mbar, which means there is practically no medium transmitting acoustic signals to the microphone. Therefore, signals must be caused by structure-borne transmission or impact of propellant.

From the spectrogram it can be learned that the acoustic signal generated by the defocused thruster system (laser operation # ≤ 80) is actually picked up as a very small signal at 400 Hz, 800 Hz, etc. between second 0 and 280 (emphasized at seconds 230 to 250 in [Fig. 8](#) in the middle). As soon as the focus is redirected onto the surface of the propellant, the signal strength rises significantly and again resonances as multiples of approximately 400 Hz (413 Hz as set up in the system) can be identified indicating that ablation takes place and generates an audio signal by striking the membrane of the microphone. At second 352 (four seconds before second 356) the laser is switched on, which partially can be seen as a barely visible signal at 826 Hz in the emphasized plot in [Fig. 8](#) to the right. Only after focussing onto the surface a strong signal unfolds. Due to evacuation the microphone exhibits a strong resonance at 4000 Hz which can be damped strongly by a high $Q = 50$ notch filter at 4009 Hz. Background noise from the vacuum pump can be seen and heard below 230 Hz. At second 495 the pump was switched off and the signal disappears. For comparison a compressed audio file can be found in [Dataset 1](#) [25].

4. Discussion

In order to ensure the function of the fully assembled system and to find possible problems the electro-optical components - liquid lens, MEMS scanner and laser diode - were characterized independently.

The liquid lens reaches a focus range of 6.5 mm (compare parameter d in Fig. 3 a)) which is larger than expected from the specification by the manufacturer. Furthermore, the measured MTF of the test assembly is slightly lower than in the simulation, which neglected the camera objective, but still confirms a sufficient image quality.

The MEMS scanner allows deflection angles of up to $\pm 4.13^\circ$ and $\pm 3.57^\circ$ on x- and y-axis controlled by a PWM duty cycle. The amplitude follows the overlap of the sinusoidal scanner oscillation and the rectangular PWM signal with little higher harmonic contribution (compare fit function Fig. 6(b)). The possible scan patterns are elliptical Lissajous figures with variable phase shift and independent amplitudes for both axes.

The laser diode works at peak powers of up to 4 W after collimation and beam forming at 1000 Hz repetition rate and $10 \mu\text{s}$ pulse length. Higher repetition rates and pulse lengths are possible but cause lower optical peak power. Attempts to achieve higher peak powers lead to instabilities of the LD-driver circuit. Peak powers close to 3 W were measured at the target plane with the whole optical system working in between. Utilizing the simulation results of the optical system from Table 2 would suggest fluences in the range of 10 J/cm^2 . This does not account for the AOI of approximately 45° , the transmission losses and the beam quality of the laser diode itself. In a worst-case calculation with $M^2 = 2.6$ the fluence is reduced to 0.75 J/cm^2 . Nevertheless, at these power levels $M^2 \approx 1.7$ should be expected, which additionally will be asymmetric due to the typical $M^2 \leq 1.3$ of the fast axis [26]. This would result in a fluence of 2.4 J/cm^2 .

All components did function under vacuum conditions as expected. Nevertheless, their suitability to space conditions introducing thermal, vacuum and radiation stress still has to be verified. Furthermore, on board diagnostics documenting the current state of the system via telemetry are likely to be necessary for a prolonged usage of this type of laser ablative thruster arrangement.

After getting hints on ablation at atmospheric pressure, we measured an audio signal correlated to the laser operation at fine vacuum as low as 2×10^{-3} mbar. Because of the low pressure and a silent thruster for defocused operation, this signal cannot be of acoustic nature and therefore has to be caused by ablated target material. This result proves the laser ablation capability of the device as well as its optical and electronic function at low pressures. It also demonstrates the performance of the almost completely 3D printed integrated optical setup using a current commercial 3D printer. Due to the long laser pulses and the fixed scanning frequency the ablation process can only be controlled via laser voltage and pulse length, which should be kept constant in order to get a preferably uniform laser energy deposition on the target. To regain this degree of freedom, a laser diode providing shorter pulses with the same pulse energy or a non-resonant scanning device with comparable energy consumption would be needed. Non-resonant operation of the MEMS scanner used in this system was only possible with more than 2.5 W power supply for scanner operation only, which did not fulfill the power requirements.

Thrust measurements with our thrust balance did not yield interpretable results. There are two possible explanations for this result. One explanation could be the ablative thrust being too small to be detected. The other explanation could be the pulsed electric nature of the laser current to interfere with the sensitive capacitive distance sensor of the thrust balance. In any case we were not able to deduce thrust with this method, despite the successful verification of laser ablation with the microphone setup. In previous laboratory experiments and simulations [11,12,27–29] it was shown, that high ISP in the order of multiple 100 s to 1000 s and thrust in the order of multiple $10 \mu\text{N}$ per Watt of laser power is possible with laser ablative thrusters.

The exact values depend strongly on the pulse duration, the propellant in use and the laser pulse energy. Here we were able to demonstrate an approach to transfer these laboratory systems into an integrated optical setup for future developments. This transfer is dominantly limited by the laser dimensions. Therefore, one next logical step could include the implementation of a small ns-laser system as e.g. a microchip DPSS laser replacing the laser diode.

The total power consumption of the demonstrated system is below 1 W with the laser only consuming 400 mW, which shows that there is potential to triple the laser output power by optimizing the laser driver electronics, especially the current supply via the buck converter. This optimization as well as future development of short pulsed laser diodes would allow ablation of a wider range of target materials and solve the scanner problem.

Besides laser propulsion, the system as a technology platform has a broad variety of applications and could possibly be used as a portable laser lab for laser material detection and inspection or as an in-situ material source for pulsed laser deposition. With some changes one could also use the system for laser communication.

Developing such a device is strongly dependent on state of the art laser diodes and electro-optical components like liquid lenses and MEMS scanners as well as the possibility of rapid prototyping using a 3D-printer. Due to the requirements of low power consumption and volume combined with high beam quality and laser peak power for propulsion the system became quite complex. There are no off-the-shelf solutions and it probably will take several years for laser technology to develop a suitable and more effective laser source in order to exploit the full potential of the system.

In any case the idea of a monolithic, 3D-printed mount for small integrated optical systems proved to be not only feasible but very promising. Manufacturers could offer CAD libraries of 3D-printable mounts for their optical components which then could be used to generate and print the opto-mechanics as a modular system directly from the optical design.

5. Conclusion

In this paper we were able to demonstrate the integration of a laser and a beam-steering setup under severe size and power limitations. This was achieved by utilizing a liquid lens, a tapered laser diode and a MEMS scanner. By these means it was possible to locally ablate material which is the essential process to create laser ablative thrust. This configuration as a technology platform allows to introduce iterative improvements to an actual laser ablative thruster design.

Acknowledgments. We want to thank Samantha Rose Siegert for proof reading the manuscript.

Disclosures. The authors declare no conflicts of interest.

Data Availability. Audio and video data underlying the results presented in this paper are available in supplementary audio [Dataset 1](#), Ref. [25] and [Visualization 1](#), Ref. [24]. Further technical details and documentation are not publicly available at this time but may be obtained from the authors upon reasonable request.

References

1. G. Raciukaitis, M. Brikas, P. Gecys, B. Voisiat, and M. Gedvilas, "Use of high repetition rate and high power lasers in microfabrication: How to keep the efficiency high?" *J. Laser Micro/Nanoeng.* **4**(3), 186–191 (2009).
2. B. N. Chichkov, C. Momma, S. Nolte, F. Von Alvensleben, and A. Tünnermann, "Femtosecond, picosecond and nanosecond laser ablation of solids," *Appl. Phys. A* **63**(2), 109–115 (1996).
3. B. Jaeggi, B. Neuenschwander, M. Schmid, M. Murali, J. Zuercher, and U. Hunziker, "Influence of the pulse duration in the ps-regime on the ablation efficiency of metals," *Phys. Procedia* **12**, 164–171 (2011).
4. R.-A. Lorbeer, J. Pastow, M. Sawanna, P. Klinkenberg, D. J. Förster, and H.-A. Eckel, "Power spectral density evaluation of laser milled surfaces," *Materials* **11**(1), 50 (2017).
5. D. Hampf, F. Sproll, P. Wagner, L. Humbert, T. Hasenohr, and W. Riede, "First successful satellite laser ranging with a fibre-based transmitter," *Adv. Space Res.* **58**(4), 498–504 (2016).
6. M. Wilkinson, U. Schreiber, I. Procházka, C. Moore, J. Degnan, G. Kirchner, Z. Zhongping, P. Dunn, V. Shargorodskiy, M. Sadovnikov, C. Courde, and H. Kunitomi, "The next generation of satellite laser ranging systems," *J. of Geodesy* (2018).

7. Z. Földes-Papp, U. Demel, and G. P. Titz, "Laser scanning confocal fluorescence microscopy: an overview," *Int. Immunopharmacol.* **3**(13-14), 1715–1729 (2003).
8. J. F. De Boer, R. Leitgeb, and M. Wojtkowski, "Twenty-five years of optical coherence tomography: the paradigm shift in sensitivity and speed provided by fourier domain oct," *Biomed. Opt. Express* **8**(7), 3248–3280 (2017).
9. J. Poliak, R. M. Calvo, and F. Rein, "Demonstration of 1.72 tbit/s optical data transmission under worst-case turbulence conditions for ground-to-geostationary satellite communications," *IEEE Commun. Lett.* **22**(9), 1818–1821 (2018).
10. Y.-C. Chi, D.-H. Hsieh, C.-T. Tsai, H.-Y. Chen, H.-C. Kuo, and G.-R. Lin, "450-nm gan laser diode enables high-speed visible light communication with 9-gbps qam-ofdm," *Opt. Express* **23**(10), 13051–13059 (2015).
11. C. Phipps, M. Birkan, W. Bohn, H.-A. Eckel, H. Horisawa, T. Lippert, M. Michaelis, Y. Rezunkov, A. Sasoh, W. Schall, S. Scharring, and J. E. Sinko, "Laser-ablation propulsion," *J. Propul. Power* **26**(4), 609–637 (2010).
12. S. Scharring, R.-A. Lorbeer, and H.-A. Eckel, "Numerical simulations on laser-ablative micropropulsion with short and ultrashort laser pulses," *T. of the Jpn. Soc. for Aeronaut. and S., Aerospace Technology Japan* **14**(30), 69–75 (2016).
13. S. Scharring, R. Lorbeer, S. Karg, L. Pastuschka, D. Förster, and H. Eckel, "The microlas concept: precise thrust generation in the micronewton range by laser ablation," in *IAA Book Series on Small Satellite* (2016).
14. R.-A. Lorbeer, S. Scharring, S. Karg, J. Pastow, L. Pastuschka, D. J. Förster, and H.-A. Eckel, "Thrust noise minimization in long-term laser ablation of propellant material in the nanosecond and picosecond regime," *Opt. Eng.* **56**(1), 011010 (2016).
15. D. Bock and M. Tajmar, "Highly miniaturized feep propulsion system (nanofeep) for attitude and orbit control of cubesats," *Acta Astronaut.* **144**, 422–428 (2018).
16. A. Kramer, P. Bangert, and K. Schilling, "UWE-4: First Electric Propulsion on a 1U CubeSat–In-Orbit Experiments and Characterization," *Aerospace* **7**(7), 98 (2020).
17. P. Friedmann, J. Gilly, J. Schleife, C. Giesin, S. Moritz, M. Herbstritt, M. Fatscher, and M. T. Kelemen, "High efficiency frequency stabilized tapered amplifiers with improved brightness," in *High-Power Diode Laser Technology and Applications IX*, vol. 7918 (International Society for Optics and Photonics, 2011), vol. 7918, p. 79180B.
18. P. Resneau, M. Garcia, M. Lecomte, Y. Robert, E. Vinet, O. Parillaud, M. Krakowski, and D. Boiko, "High performances of very long (13.5 mm) tapered laser emitting at 975 nm," in *Novel In-Plane Semiconductor Lasers XV*, vol. 9767 (International Society for Optics and Photonics, 2016), vol. 9767, p. 97671J.
19. F. Romero, A. Salinas-Castillo, A. Rivadeneyra, A. Albrecht, A. Godoy, D. Morales, and N. Rodriguez, "In-depth study of laser diode ablation of kapton polyimide for flexible conductive substrates," *Nanomaterials* **8**(7), 517 (2018).
20. M. Zohrabi, R. H. Cormack, and J. T. Gopinath, "Wide-angle nonmechanical beam steering using liquid lenses," *Opt. Express* **24**(21), 23798–23809 (2016).
21. W. Kim, H. C. Yang, and D. S. Kim, "Wide and fast focus-tunable dielectro-optofluidic lens via pinning of the interface of aqueous and dielectric liquids," *Opt. Express* **25**(13), 14697–14705 (2017).
22. A. Wolter, S. T. Hsu, H. Schenk, and H. K. Lakner, "Applications and requirements for mems scanner mirrors," in *MOEMS and Miniaturized Systems V*, vol. 5719 (International Society for Optics and Photonics, 2005), vol. 5719, pp. 64–76.
23. C. D. Lu, M. F. Kraus, B. Potsaid, J. J. Liu, W. Choi, V. Jayaraman, A. E. Cable, J. Hornegger, J. S. Duker, and J. G. Fujimoto, "Handheld ultrahigh speed swept source optical coherence tomography instrument using a mems scanning mirror," *Biomed. Opt. Express* **5**(1), 293–311 (2014).
24. T. Bauer, S. Weixler, R.-A. Lorbeer, and H.-A. Eckel, "Thermal glow from laser ablation in air," figshare (2021) [retrieved 26 January 2021], <https://doi.org/10.6084/m9.figshare.14170529>.
25. T. Bauer, S. Weixler, R.-A. Lorbeer, and H.-A. Eckel, "Audio stream generated during vacuum ablation test at a pressure between 0.2 to 0.3 Pa," figshare (2021) [retrieved 26 January 2021], <https://doi.org/10.6084/m9.figshare.13643297>.
26. M. Chi, A. Müller, A. K. Hansen, O. B. Jensen, P. M. Petersen, and B. Sumpf, "Microsecond pulse-mode operation of a micro-integrated high-power external-cavity tapered diode laser at 808 nm," *Appl. Opt.* **59**(26), 7836–7840 (2020).
27. C. Phipps, J. R. Luke, T. Lippert, M. Hauer, and A. Wokaun, "Micropropulsion using a laser ablation jet," *J. Propul. Power* **20**(6), 1000–1011 (2004).
28. C. R. Phipps, J. R. Luke, and W. D. Helgeson, "3ks specific impulse with a ns-pulse laser microthruster," Tech. rep., PHOTONIC ASSOCIATES SANTA FE NM (2005).
29. A. Gurin, K. Y. Kuvaev, E. Y. Loktionov, Y. S. Protasov, K. Sirenko, and V. Zakharov, "First attempt of a laser thruster space flight test: Lost at launch," *Opt. Laser Technol.* **120**, 105656 (2019).